PHYSICAL REVIEW MATERIALS **3**, 084406 (2019)

Multiscale simulations toward calculating coercivity of Nd-Fe-B permanent magnets at high temperatures

Qihua Gong,[1] Min Yi,[1,2,3,*] and Bai-Xiang Xu[1]
[1] *Institute of Materials Science, Technische Universität Darmstadt, 64287 Darmstadt, Germany*
[2] *State Key Laboratory of Mechanics and Control of Mechanical Structures, and Key Laboratory for Intelligent Nano Materials and Devices, Ministry of Education and College of Aerospace Engineering, Nanjing University of Aeronautics and Astronautics (NUAA), Nanjing 210016, China*
[3] *State Key Laboratory for Strength and Vibration of Mechanical Structure, Xi'an Jiaotong University, Xi'an 710049, China*

(Received 7 March 2019; published 9 August 2019)

A computational scheme integrating the atomistic spin model (ASM) and micromagnetic simulations is proposed to predict the coercivity of Nd-Fe-B permanent magnets at high temperatures. ASM simulations are applied to calculate the temperature-dependent intrinsic parameters of $Nd_2Fe_{14}B$, including the saturated magnetization, magnetocrystalline anisotropy, and exchange stiffness, which are shown to agree well with the experimental values. With the ASM results as input, finite-temperature micromagnetic simulations based on the stochastic Landau-Lifshitz-Gilbert equation are performed to calculate the magnetic reversal and coercivity (H_c) at high temperatures. It is found that in addition to the decrease of anisotropy field with temperature, thermal fluctuations further reduce H_c by 5–10% and β (temperature coefficient of coercivity) by 0.02–0.1% K^{-1} in the presence of a defect layer. The computed thermal-activation volume, which increases with temperature, is shown to be enhanced by several times due to the defect layer with strong magnetization (e.g., 1 T), but can be decreased by introducing a hard shell. Both H_c and β can be enhanced by adding the Dy-rich shell, but saturate at a shell thickness (t^{sh}) around 6–8 nm after which further increasing t^{sh} or adding Dy into the core is not essential.

DOI: 10.1103/PhysRevMaterials.3.084406

I. INTRODUCTION

Nd-Fe-B permanent magnets, which were discovered in 1984 [1,2], have been widely used in modern technology such as motors, wind turbines, and memory devices due to their excellent magnetic properties. Those magnets are required to retain its functionality at high temperatures in many applications. For example, the operating temperature of Nd-Fe-B magnets can approach 350 and 450 K in the wind turbines and motors inside electric and hybrid vehicles, respectively. Therefore, increasing thermal stability, and understanding and predicting the temperature dependence of magnetic properties, is of great significance in the design of Nd-Fe-B permanent magnets for the applications at high temperatures.

In order to increase the thermal stability of Nd-Fe-B permanent magnets, up to now diverse methods have been tried. The effects of the alloying elements Co, Dy, Al, Nb, Zr, Cu, Gd, etc. on the high-temperature properties of sintered Nd-Fe-B magnets have been explored [3,4]. The most efficient way to increase thermal stability is the partial substitution of Nd with heavy rare earth (HRE) such as Dy and Tb [5,6] since $(Nd, HRE)_2Fe_{14}B$ possesses a higher intrinsic anisotropy field. However, due to the limited supply and high cost of HRE, the community of permanent magnets makes great efforts to reduce the usage amount of HRE or totally remove HRE. In this respect, hot deformation is shown to achieve an improved temperature coefficient of coercivity (β) in HRE-free Nd-Fe-B magnets, owing to the finer grains and thus smaller local demagnetization field [7]. Alternatively, grain-boundary diffusion of Nd-Cu [8] and Pr-Cu alloys [9] in HRE-free Nd-Fe-B magnets also enhances β. However, for high-end applications such as electromobility where the temperature can approach 450 K, the addition of HRE is still necessary. In order to reduce the HRE usage amount, HRE is not added to the main phase during the alloying step, but is diffused along the grain boundary of Nd-Fe-B magnets to form a thin HRE-rich hard shell around the main phase $Nd_2Fe_{14}B$. [10–13]. Nevertheless, continuous efforts toward HRE-free Nd-Fe-B magnets with excellent performance at high temperatures never stop.

Apart from the experimental efforts to enhance the high-temperature performance of Nd-Fe-B magnets, theoretical models and computational methodology have also been very helpful in terms of reducing the research cost and accelerating the design process. Currently, three modeling and simulation techniques are available for the theoretical and computational study of Nd-Fe-B magnets. First-principles calculations are important for the prediction of intrinsic magnetic parameters of the $Nd_2Fe_{14}B$ phase and some subphases in Nd-Fe-B magnets at 0 K and the associated physical mechanism at the electronic level [14–19]. But it is still challenging to directly apply first principles for the calculation of finite-temperature properties of Nd-Fe-B magnets. Recently, the atomistic spin model (ASM) has been utilized to calculate the temperature-dependent intrinsic parameters of $Nd_2Fe_{14}B$ [20–27]. ASM is based on a spin Hamiltonian and can be parameterized by

---

[*] yimin@nuaa.edu.cn

the input from first principles. Generally, ASM is capable of calculating magnetic parameters at different temperatures by considering temperature effects via Langevin-like spin dynamics or Monte Carlo scheme [28–30]. Due to its intrinsic scale at the atomic level, ASM works well for nanomagnets, but is less powerful when the microstructure is considered. In the analysis of the experimental hysteresis and the simulation of magnetic domain reversal and microstructural influences, the micromagnetic model plays an important role and is already widely used [31–42].

Based on the micromagnetic nucleation model, the coercivity of Nd-Fe-B magnets is often expressed as $H_\mathrm{c}(T) = \alpha_\mathrm{k}H_\mathrm{k}(T) - N_\mathrm{eff}M_\mathrm{s}(T) - H_\mathrm{th}(T)$ [43], where the coefficients α_k represents the microstructural influence on the anisotropy field and N_eff is related to the effect of the microstructure-sensitive local demagnetization factor. Efforts to tune the microstructure such as grain boundary, hard shell, intergranular phase, and texture contribute to the increase of α_k [8–13,31, 35–40,44]. The work on grain size or shape is actually related to the tailoring of N_eff [7,31–33,45–49]. $H_\mathrm{th}(T)$ gives the reduction of coercivity by the temperature-induced thermal fluctuations. It should be noted that this thermal fluctuation related to $H_\mathrm{th}(T)$ is exerted on the macrospin or magnetization vector in terms of micromagnetic theory, whereas the thermal fluctuation in ASM is exerted on the atomistic spin. According to the above expression for $H_\mathrm{th}(T)$, the temperature-dependent H_k, M_s, and H_th play a decisive role in the coercivity of Nd-Fe-B magnets at finite temperatures.

As mentioned above, experimental results or first-principles-informed ASM provide a feasible way to calculate temperature-dependent H_k and M_s. But the application of ASM to permanent magnets or, more specifically, rare-earth permanent magnets is still in its infancy. For the estimation of H_th influence, micromagnetic simulations are indispensable and there are two different choices depending on how the temperature-induced thermal fluctuations are taken into account. One choice is to compute the energy barrier as a function of the applied field by micromagnetic simulations without the consideration of thermal fluctuations. When the energy barrier is equal to the thermal energy $25k_\mathrm{B}T$, the corresponding external magnetic field is defined as the thermal coercivity at temperature T. For the calculation of the energy barrier, the elastic band method [50–52] or the string method [53–56] is often utilized. Recently, Schrefl *et al.* applied this method to calculate the temperature-dependent coercivity and thermal activation of magnetic reversal in Nd-Fe-B permanent magnets [37,41,42,57]. The alternative choice for dealing with the temperature influence and thermal activation in the magnetic reversal process is to add a stochastic term into the effective magnetic field in the Landau-Lifshitz-Gilbert (LLG) equation, leading to the stochastic LLG equation [58]. The strength of the stochastic term is related to temperature. Numerical implementation of the stochastic LLG equation makes it possible to study the thermally activated magnetization reversal and the temperature influence on switching dynamics by micromagnetic simulations [59–64]. But its application to rare-earth permanent magnets is still rare.

From the viewpoint of modeling and simulation, no individual methodology is applicable for simultaneously calculating all the three terms H_k, M_s, and H_th at different temperatures to evaluate the temperature-dependent coercivity of Nd-Fe-B magnets. To this end, we present a multiscale scheme by combining ASM and micromagnetic simulations for the computational prediction of the coercivity of Nd-Fe-B permanent magnets at high temperatures. We construct the ASM Hamiltonian for $\mathrm{Nd_2Fe_{14}B}$ and calculate the temperature-dependent intrinsic material parameters of $\mathrm{Nd_2Fe_{14}B}$, including the saturated magnetization (M_s), the magnetocrystalline anisotropy (K_1), and the exchange stiffness constant (A_e). Taking the calculated $M_\mathrm{s}(T)$, $K_1(T)$, and $A_\mathrm{e}(T)$ as input, micromagnetic simulations based on the stochastic LLG equation are performed to reveal the temperature influence on the coercivity of Nd-Fe-B magnets. The representative microstructural features including surface defect and Dy-rich hard shell are also explored to reveal their influences on the coercivity at high temperatures.

II. METHODOLOGY

A. Atomistic spin model simulation

ASM simulation is used to calculate the temperature-dependent intrinsic magnetic parameters of the $\mathrm{Nd_2Fe_{14}B}$ phase with the space group of $P4_2/mnm$, 68 atoms per unit cell, and a ferromagnetic ground state. ASM treats each atom as a classic spin [28–30]. For the special case of $\mathrm{Nd_2Fe_{14}B}$, the ASM Hamiltonian can be written as [21–23,27]

$$\mathcal{H} = -\frac{1}{2}\sum_{i\neq j}^{i,j\in\mathrm{Fe}} J_{ij}^{\text{Fe-Fe}}\mathbf{s}_i\cdot\mathbf{s}_j - \sum_{i\in\mathrm{Fe}}^{j\in\mathrm{Nd}} J_{ij}^{\text{Fe-Nd}}\mathbf{s}_i\cdot\mathbf{s}_j - \sum_{i\in\mathrm{Fe}} k_i^{\mathrm{Fe}}(\mathbf{s}_i\cdot\mathbf{e}^z)^2 + \mathcal{H}_{\mathrm{Nd}}^{\mathrm{cf}}. \tag{1}$$

Here the calculation of intrinsic parameters is the focus, so the energy terms related to the external magnetic field and the dipole interaction between atomic spin moments are not included in Eq. (1). Here, $\mathbf{s}_i$ is a unit vector denoting the local spin moment direction. In Eq. (1), the first two terms are the Heisenberg exchange energies, which only contain the exchange interactions in Fe-Fe ($J_{ij}^{\text{Fe-Fe}}$) and Fe-Nd ($J_{ij}^{\text{Fe-Nd}}$) atomic pairs. The B sites are usually taken to be nonmagnetic and the interaction between Nd sites can be negligible [21–23]. The third term corresponds to the uniaxial magnetic anisotropy energy of Fe atoms, with k_i^{Fe} as the anisotropy energy per Fe atom and $\mathbf{e}^z$ the z-axis unit vector. The fourth term denotes the crystal-field (CF) Hamiltonian of Nd ions, which is the main source of large magnetic anisotropy of $\mathrm{Nd_2Fe_{14}B}$ and can be approximated as [21,22,65]

$$\mathcal{H}_{\mathrm{Nd}}^{\mathrm{cf}} = \sum_{i\in\mathrm{Nd}}\sum_{n=2,4,6}\alpha_n\langle r^n\rangle_{4f,i}A_{n,i}^0\hat{\Theta}_{n,i}^0, \tag{2}$$

in which α_n is the Stevens factors, $\langle r^n\rangle_{4f,i}$ is the $4f$ radial expectation value of r^n at the respective Nd site i, $A_{n,i}^0$ are the CF parameters, and $\hat{\Theta}_{n,i}^0$ are the Stevens operator equivalents whose detailed expressions can be found in [66]. For Nd^{+3} ions, $\alpha_2 = -6.428\times10^{-3}$, $\alpha_4 = -2.911\times10^{-4}$, and $\alpha_6 = -3.799\times10^{-5}$ [66]. The $\langle r^n\rangle$ values of Nd^{+3} ions can be calculated as $\langle r^2\rangle = 1.001a_0^2$, $\langle r^4\rangle = 2.401a_0^4$, and $\langle r^6\rangle = 12.396a_0^6$, in which a_0 is the Bohr radius [67]. The reliable first-principles calculation of high-order CF parameters in

TABLE I. Magnetic moments and atomic-site resolved magnetic anisotropy energy of each crystallographically equivalent atom.

Atom	μ_i (μ_B)	k_i ($\times 10^{-21}$ J)
		k_i^Nd
Nd(4g)	2.86	$k_{i,1}^\mathrm{Nd} = -4.935$ $k_{i,2}^\mathrm{Nd} = 25.98$ $k_{i,3}^\mathrm{Nd} = -22.94$
Nd(4f)	2.871	
		k_i^Fe
Fe(4c)	2.531	−0.342
Fe(4e)	1.874	−0.0048
Fe(8j_2)	2.629	0.093
Fe(8j_1)	2.298	0.171
Fe(16k_2)	2.206	0.0608
Fe(16k_1)	2.063	0.0880

$Nd_2Fe_{14}B$ is still challenging. Here we take the A_n^0 values which are determined from the experiment results [65], i.e., $A_2^0 = 295\ \mathrm{K}/a_0^2$, $A_4^0 = -12.3\ \mathrm{K}/a_0^4$, and $A_6^0 = -1.84\ \mathrm{K}/a_0^6$. We approximately set all Nd ions with the same CF parameters. Substituting the expressions of $\hat{\Theta}_{n,i}^0$ [66] into (2) yields the CF energy as

$$\mathcal{H}_\mathrm{Nd}^\mathrm{cf} = -\sum_{i\in\mathrm{Nd}} \left[k_{i,1}^\mathrm{Nd}(\mathbf{s}_i\cdot\mathbf{e}^z)^2 + k_{i,2}^\mathrm{Nd}(\mathbf{s}_i\cdot\mathbf{e}^z)^4 + k_{i,3}^\mathrm{Nd}(\mathbf{s}_i\cdot\mathbf{e}^z)^6\right]. \tag{3}$$

The parameters $k_{i,1}^\mathrm{Nd}$, $k_{i,2}^\mathrm{Nd}$, and $k_{i,3}^\mathrm{Nd}$ are listed in Table I. The constant term in $\mathcal{H}_\mathrm{Nd}^\mathrm{cf}$ is not important and thus not presented in Eq. (3). The magnetocrystalline anisotropy energy of the Fe sublattice and the magnetic moments of each atom, as listed in Table I, are taken from the previous first-principles calculations [21,68]. The exchange parameters $J_{ij}^\mathrm{Fe\text{-}Fe}$ and $J_{ij}^\mathrm{Fe\text{-}Nd}$ in Eq. (1) are taken from the previous calculations based on the Green's function method and the magnetic-force theorem by using OPENMX [27,69–71]. J_{ij}, in both cases of nearest neighbor and 9 Å cutoff, is calculated, as shown in Fig. 1. It can be found that beyond the nearest neighbor, the Fe-Nd exchange almost vanishes, while the Fe-Fe exchange is small and oscillates. The long-range behavior of Fe-Fe exchange is also reported in [72]. In order to reduce computational costs, as a simplification, sometimes only the exchange parameters within the nearest neighbor are used. In the case here for $Nd_2Fe_{14}B$, we show in the following that the calculated intrinsic parameters from this simplification agree well with the experimental report (Fig. 3) [73–75], and the disparity between using nearest-neighbor and 9-Å-cutoff J_{ij} is small (Figs. 3 and 4).

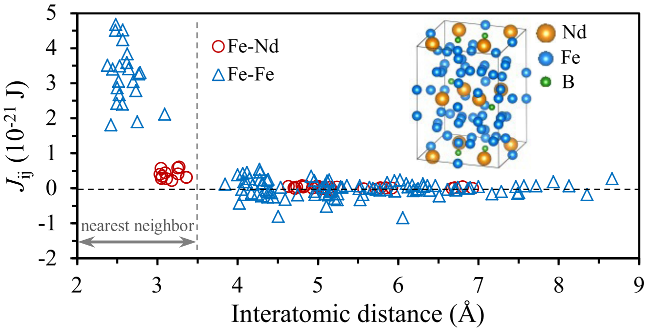

FIG. 1. Exchange parameters J_{ij} as a function of interatomic distance, with the nearest-neighbor range marked. Inset: unit cell of $Nd_2Fe_{14}B$.

It should be noted that the noncollinearity of the magnetic configuration is shown to significantly influence the exchange parameters, as reported in [76,77]. However, in our case $Nd_2Fe_{14}B$ here, it has been verified that the angle difference between the total magnetization and the Fe/Nd magnetization is extremely low over the entire temperature range [78], especially in temperatures higher than 300 K considered here. Thus, the noncollinearity effect here is negligibly small. Therefore, calculating J_{ij} (Fig. 1) in $Nd_2Fe_{14}B$ by assuming the collinearity is reasonable.

After parametrization, the ASM in Eq. (1) is implemented in VAMPIRE [29]. For the calculation of $M_\mathrm{s}(T)$, the Monte Carlo Metropolis method is used. After performing 10 000 Monte Carlo steps at each temperature, the equilibrium properties of the system are calculated by averaging the magnetic moments over a further 10 000 steps. The results are confirmed to remain the same when the Monte Carlo steps exceed 10 000. For the calculation of $K_1(T)$, the constrained Monte Carlo method is used [29,79]. The direction of the global magnetization at a fixed polar angle (θ) is constrained, while the individual spins are allowed to rotate. In this way, the energy as a function of θ can be obtained. A_e is estimated at high temperatures through the relationship $\delta_w = \pi\sqrt{A_\mathrm{e}/K_1}$ [80]. δ_w denotes the domain-wall width, which is calculated by applying the spin dynamics approach and the Heun integration scheme. A sharp Bloch-like domain wall (wall plane perpendicular to the x axis) in the middle of the sample with 40×5×5 unit cells is set as the initial condition. The system with the demagnetizing field included further relaxes from this initial condition by 100 000 steps with a time step of 1 fs. The final domain configuration is determined by averaging the magnetic moment distribution of 100 states at 90.1, 90.2, 90.3, …, 100 ps.

B. Micromagnetic simulation

In contrast to the ASM at the atomistic spin scale, the micromagnetic model is a continuum theory that disentangles the magnetization process on the length scale of magnetic domain and domain walls [81]. The magnetic state is described by the magnetization $\mathbf{M} = \mathbf{m}M_\mathrm{s}$, with $\mathbf{m}$ as the unit vector for the magnetization direction. For Nd-Fe-B magnets with the uniaxial magnetic anisotropy, the magnetic Gibbs energy is expressed as

$$E(\mathbf{m},T) = \int_\Omega \Big\{A_\mathrm{e}(T)\|\nabla\mathbf{m}\|^2 + K_1(T)[1-(\mathbf{m}\cdot\mathbf{e}^z)^2] - \frac{1}{2}\mu_0 M_\mathrm{s}(T)\mathbf{m}\cdot\mathbf{H}_\mathrm{d} - \mu_0 M_\mathrm{s}(T)\mathbf{m}\cdot\mathbf{H}_\mathrm{ext}\Big\}dv. \tag{4}$$

The spatial distribution of the temperature-dependent exchange stiffness $A_\mathrm{e}(T)$, magnetocrystalline anisotropy $K_1(T)$, and magnetization saturation $M_\mathrm{s}(T)$ represents the microstructure of Nd-Fe-B magnets. In micromagnetic simulations, the demagnetization field is included. $\mathbf{H}_\mathrm{d}$ and $\mathbf{H}_\mathrm{ext}$ denote the demagnetization field and external magnetic field, respectively.

The magnetization dynamics are described by the LLG equation [82,83],

$$\dot{\mathbf{m}} = -\frac{\gamma}{1+\alpha^2}[\mathbf{m}\times\mathbf{H}_\mathrm{eff} + \alpha\mathbf{m}\times(\mathbf{m}\times\mathbf{H}_\mathrm{eff})], \qquad (5)$$

where γ denotes the gyromagnetic ratio, α the dimensionless Gilbert damping parameter, and $\mathbf{H}_\mathrm{eff} = -\frac{1}{M_\mathrm{s}}\frac{\delta E}{\delta \mathbf{m}}$ the effective field. The finite-temperature effect is modeled by adding a fluctuating thermal field $\mathbf{H}_\mathrm{therm}$ into $\mathbf{H}_\mathrm{eff}$, so that a stochastic LLG (sLLG) equation is obtained. According to Brown [58], the thermal field can be expressed as

$$\mathbf{H}_\mathrm{therm} = \boldsymbol{\eta}\sqrt{\frac{2\alpha k_\mathrm{B}T}{M_\mathrm{s}(T)\gamma\,\Delta V\,\Delta t}}, \qquad (6)$$

in which $\boldsymbol{\eta}$ is a random vector from a standard normal distribution and is regenerated after every time step. ΔV is the single-cell volume and Δt is the time step. In general, $\mathbf{H}_\mathrm{therm}$ has zero average and is uncorrelated both in time and space. The stochastic LLG equation is solved in MUMAX3 [84,85] by using the Heun integration method and a fixed time step, which will be optimized in the following to reduce the computation cost. Therefore, there are five kinds of energy being considered in micromagnetics, which are exchange energy, anisotropy energy, Zeeman energy, demagnetization energy, and thermal energy. For the calculation of magnetic reversal curves, $\mathbf{H}_\mathrm{ext}$ is applied as a stepwise field.

The dodecahedral grain model, as an approximation of the polyhedral geometry of grains observed in actual Nd-Fe-B permanent magnets, is used in this work. For the dodecahedral grain, we use an open boundary condition, not a periodic boundary condition. In the current work, we focus on the single grain. Since there are already previous micromagnetic studies on the similar single grain [41,42], it is convenient for us to compare our micromagnetic results with previous ones and thus verify our method. The single grain is not realistic here, but a model to verify the proposed multiscale scheme. The multigrain case will be studied later. Typical microstructures such as the magnetically soft grain-boundary phase (modeled as a defect layer) and grain-boundary diffused Dy-rich layer (modeled as a hard shell) are also considered. They provide the possibility of improving the coercivity of Nd-Fe-B permanent magnets by microstructure engineering, while alleviating the risk of the heavy-rare-earth crisis. Namely, three kinds of models based on the single dodecahedral grain are built here: (a) a pure $Nd_2Fe_{14}B$ grain without defect or hard shell; (b) a $Nd_2Fe_{14}B$ grain covered with a 3-nm-thick defect layer; (c) a $Nd_2Fe_{14}B$ core with a hard $(Nd_{0.53}Dy_{0.47})_2Fe_{14}B$ shell and a outer defect layer of 3 nm, as shown in Fig. 2. The diameter of the $Nd_2Fe_{14}B$ core is kept constant at 51 nm. The hard-shell thickness (t^sh) is varied to investigate its effectiveness in enhancing coercivity.

According to the ASM results on the temperature-dependent intrinsic parameters in the following, the exchange length $l_\mathrm{ex}(T) = \sqrt{2A_\mathrm{e}(T)/[\mu_0 M_\mathrm{s}^2(T)]}$ and the Bloch parameter $\delta_\mathrm{w}(T)/\pi = \sqrt{A_\mathrm{e}(T)/K_1(T)}$ at 300–550 K can be estimated and their minimum value is found to be around 1.6 nm. The finite-difference cell size should be smaller than $l_\mathrm{ex}(T)$ and $\delta_\mathrm{w}(T)/\pi$ [86] and thus is chosen to be 1.5 nm. It should be noted that in the thermal micromagnetic problems, the cell size is suggested to satisfy an additional criteria, i.e., it should be smaller than the thermal exchange length $l_\mathrm{th}(T) = \sqrt{A_\mathrm{e}(T)/[\mu_0 M_\mathrm{s}(T)\|\mathbf{H}_\mathrm{therm}(T)\|]}$ [62]. Here, in the case of Gilbert damping parameter 0.1, cell size 1.5 nm, and time step 50 fs, the minimum $l_\mathrm{th}(T)$ at 300–550 K is estimated as 1.3 μm, which is much larger than the cell size, indicating a cell size of 1.5 nm is reasonable.

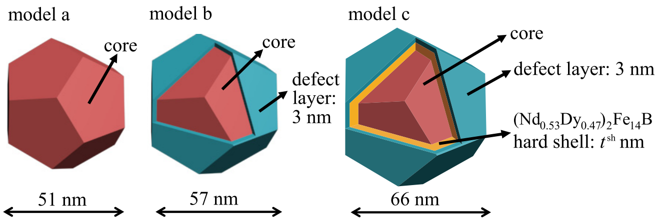

FIG. 2. Three kinds of models for micromagnetic simulations. (a) $Nd_2Fe_{14}B$ dodecahedral grain with a diameter of 51 nm. (b) $Nd_2Fe_{14}B$ grain covered with a 3 nm defect layer. (c) $Nd_2Fe_{14}B$ grain covered with $(Nd_{0.53}Dy_{0.47})_2Fe_{14}B$ hard shell (thickness t^sh) and 3 nm outer defect layer.

The temperature-dependent M_s and K_1 of the $(Nd_{1-x}Dy_x)_2Fe_{14}B$ hard shell (model "c" in Fig. 2) are obtained by using the experimental data [87]. $A_\mathrm{e}(T)$ of the hard shell is taken the same as that of $Nd_2Fe_{14}B$. Direct calculation of these intrinsic magnetic parameters of $(Nd_{1-x}Dy_x)Fe_{14}B$ by ASM simulations is still challenging and will be explored in the near future. In the following calculations, $(Nd_{1-x}Dy_x)_2Fe_{14}B$ with $x = 0.47$ is chosen as the hard shell.

III. RESULTS AND DISCUSSION

A. Intrinsic parameters at high temperatures

The temperature-dependent magnetization calculated by ASM simulations is shown in Fig. 3(a). It can be found that the ASM simulation results show excellent agreement with the experimental one [74]. Fitting the data in Fig. 3(a) by the Curie-Bloch equation $M_\mathrm{s}(T) = M_0[1-(T/T_\mathrm{c})^{\alpha_1}]^{\alpha_2}$ yields the Curie temperature $T_\mathrm{c} = 602$ K, parameter $\alpha_1 = 1.802$, and parameter $\alpha_2 = 0.418$.

The magnetocrystalline anisotropy is determined by calculating the system energy when the global magnetization is aligned along different directions at different temperatures. The energy density F at different temperatures is estimated by the constrained Monte Carlo method, in which the azimuthal angle is fixed at zero degree and the polar angle is gradually changed from 0 to 90 degrees. The ASM simulation results on temperature-dependent F are shown in Fig. 3(b) and can be well fitted by $F = K_1\sin^2\theta$, from which the magnetocrystalline anisotropy constant K_1 is attained. As presented in Fig. 3(c), the fitted K_1 is well in line with the experimental measurement [73].

In order to calculate the exchange stiffness A_e at high temperatures, we first determine the domain-wall width δ_w.

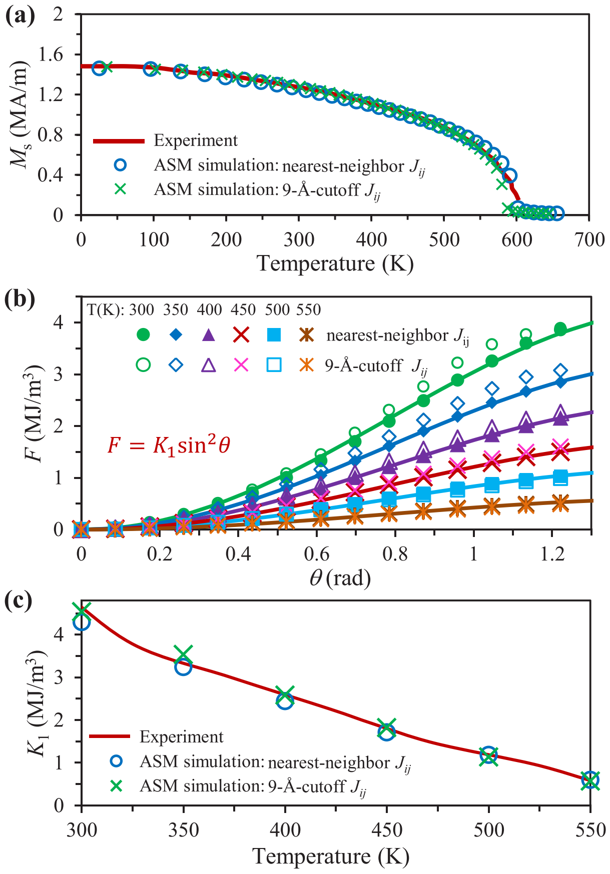

FIG. 3. ASM simulation results on (a) temperature-dependent magnetization saturation M_s, (b) free-energy density as a function of polar angle θ at high temperatures, and (c) magnetocrystalline anisotropy $K_1(T)$. The experimental results in (a) and (c) are taken from Refs. [74] and [73]. Results for both nearest-neighbor and 9-Å-cutoff J_{ij} are shown and compared.

For the calculation of δ_w, we set the magnetic moment direction in the y-z plane with a polar angle as 0 and 180° in the upward and downward domain, respectively. Then the system is relaxed to obtain the Bloch domain-wall configuration represented by the atomistic magnetic moments, as shown in Fig. 4(a). It can be seen that the domain wall is intuitively observable. As the temperature increases, the effect of thermal fluctuations is stronger and the domain wall becomes wider. In order to compute δ_w, the magnetization distribution along the x axis in Fig. 4(a) is fitted by the continuum description of the domain wall or diffusive interface, i.e., $M_z = -M_z^0 \tanh[(x - x_0)/(\delta_w/\pi)]$ [80]. The parameter M_z^0 is determined by fitting the $M_z - x$ data points which describe the domain-wall configuration. The fitted M_z^0 is found to agree well with the values in Fig. 3(a) at high temperatures. The typical fitting results at 400 K are shown in Fig. 4(b), from which δ_w is readily attained. The fitted δ_w as a function of temperature is presented in Fig. 4(c). Finally, the combination of δ_w in Fig. 4(c), K_1 in Fig. 3(c), and the relationship $\delta_w = \pi\sqrt{A_e/K_1}$ [80] yield temperature-dependent A_e, as shown in Fig. 4(d). It can be found that A_e decreases with the increasing temperature. $A_e = 10.3$ pJ/m at 300 K is also consistent with the literature report [80]. With these temperature-dependent intrinsic parameters at hand, micromagnetic simulations including the microstructure features are feasible.

It should be mentioned that the main objective of this work is to demonstrate the proof of concept, i.e., the feasibility of multiscale simulations combining the atomistic spin model (ASM) and micromagnetics to calculate the coercivity of permanent magnets at high temperatures. As a preliminary step, we take Nd-Fe-B as an example whose intrinsic parameters (M_s, K_1, and A_e) are experimentally available so that the feasibility of multiscale simulations can be verified. In the near future, the multiscale simulation methodology in this work will be extended to another set of materials whose properties are not experimentally available and thus the predictive power of the methodology will be further explored.

B. Temperature-dependent coercivity

1. Influence of stepwise external field and step time

In order to calculate the magnetic hysteresis and thus the coercivity, a stepwise external field is applied. The stepwise field is characterized by two parameters, ΔB_{ex} and t_{rB}, as illustrated in Fig. 5(a). ΔB_{ex} is the increment step of the external field. t_{rB} indicates the duration of each external field, i.e., how long an external field is kept until it is decreased by ΔB_{ex}. According to Eq. (6), it is obvious that the thermal fluctuation field is strongly influenced by the cell volume

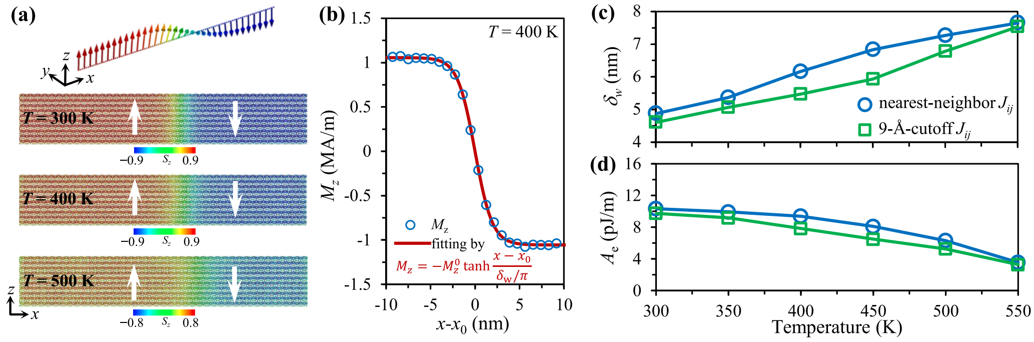

FIG. 4. ASM simulations results on (a) temperature-dependent domain-wall configuration presented by the distribution of atomistic magnetic moments, (b) M_z distribution along the x axis at $T = 400$ K, (c) domain-wall width, and (d) exchange stiffness at high temperature. Results for both nearest-neighbor and 9-Å-cutoff J_{ij} are shown and compared in (c) and (d).

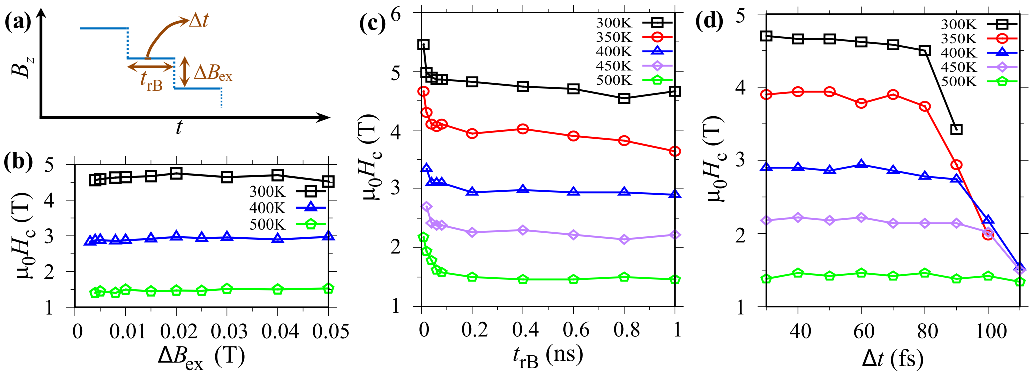

FIG. 5. (a) Schematics of applying stepwise external field for the coercivity calculation. ΔB_{ex}: increment step of the external field; Δt: step time for solving sLLG equation; t_{rB}: duration of applying a constant external field. Temperature-dependent coercivity of model "a" (Fig. 2) as a function of (b) ΔB_{ex} with fixed $t_{rB} = 0.4$ ns and $\Delta t = 50$ fs, (c) t_{rB} with fixed $B_{ex} = 0.01$ T and $\Delta t = 50$ fs, and (d) Δt with fixed $\Delta B_{ex} = 0.01$ T and $t_{rB} = 0.4$ ns.

(ΔV) and the integration time step (Δt) for solving the sLLG equation. Here we fix the cell size as 1.5 nm and thus ΔV as 1.5^3 nm^3, as mentioned in Sec. II B. In principle, smaller Δt and larger t_{rB} favor the reliable calculation of coercivity, but take more computation time. Hereby, in order to make the calculated coercivity H_c at high temperatures convincing and, at the same time, save the computation cost, we evaluate the influence of ΔB_{ex}, t_{rB}, and Δt for the three models in Fig. 2.

Figures 5(b)–5(d) shows the typical results for the case of model "a". It can be seen from Fig. 5(b) that the H_c vs ΔB_{ex} curves present very weak increasing trends when ΔB_{ex} is changed by one order of magnitude (ranging from 0.004 to 0.05 T). This indicates that H_c is not strongly influenced by ΔB_{ex}. For the following calculations, $\Delta B_{ex} = 0.01$ T is chosen. In contrast, as shown in Fig. 5(c), H_c is found to first decrease with the increasing t_{rB} and then nearly saturate at $t_{rB} = 0.2$–0.4 ns. Similarly, in Fig. 5(d), H_c decreases with the increasing Δt when Δt is above 70 fs. H_c almost saturates when Δt is reduced from 60 fs at 300–500 K. Similar results are also found for the cases of models "b" and "c." Ideally, t_{rB} should be in the scale of second, which is the typical experimental timescale for the coercivity measurement. However, t_{rB} in the order of second makes the computational cost unacceptable. Seeing that the saturation behavior of H_c with respect to both t_{rB} and Δt appears in Figs. 5(c) and 5(d), we take $\Delta t = 50$ fs and $t_{rB} = 0.4$ ns for the following micromagnetic simulations.

2. *Influence of thermal fluctuations*

At finite temperatures, the thermal activation will induce the premature nucleation and thus influence the coercivity. In micromagnetic simulations, the temperature effects should be attributed to not only the temperature-dependent intrinsic parameters, but also the finite-temperature-induced thermal fluctuations.

In order to investigate the effect of thermal fluctuations, the geometry, composition, and magnetic properties of the defect layer and hard shell are kept unchanged. As shown in model "b" (Fig. 2), the $Nd_2Fe_{14}B$ grain surface is assumed to be covered by a 3-nm-thick soft defect layer whose magnetic properties are set as $\mu_0 M_s^d = 1$ T, $A_e^d = 6.2$ pJ/m, and $K_1^d = 0$ MJ/m^3. These values for M_s^d, A_e^d, and K_1^d of the defect layer are chosen according to the experimental measurement of the ferromagnetic grain-boundary (GB) phase that is demonstrated to contain an Fe+Co content of about 60% [40]. Since the change in M_s of Fe and Co within 300–500 K is negligible [88] and the recent experimental measurement shows not too much change in the magnetization of GB phase at low temperatures [89], M_s^d of the defect layer with the main composition as Fe+Co is reasonably assumed to be temperature independent within 300–500 K. The Dy-rich hard shell is set as 3 nm thick with a composition of $(Nd_{0.53}Dy_{0.47})Fe_{14}B$ whose temperature-dependent magnetic properties can be readily extracted from the experimental measurements [87].

Figure 6 shows the typical magnetization reversal curves and the corresponding magnetic states in the three models at 400 K. It can be found from Fig. 6(a) that without thermal fluctuations, the reversal curves are smooth, while they fluctuates when temperature-induced thermal fluctuations are considered. The coercivity is also obviously reduced by thermal fluctuations. Figure 6(b) shows the separate contributions to the magnetization reversal from the $Nd_2Fe_{14}B$ core, GB defect layer, and Dy-doped hard shell for models "b" and "c." It is clear that magnetization reversal in the GB defect layer is much faster in model "b" without a hard shell than that in model "c" with a hard shell. The thermal fluctuations also induce faster magnetization reversal in the GB defect layer. In model "c," the hard shell is directly exchange coupled to the GB defect layer and thus is magnetically reversed faster than the $Nd_2Fe_{14}B$ core. At the coercivity point, the total magnetization in core, GB, and shell is reversed instantly. The representative magnetic states during the magnetization reversal process at the coercivity point are shown in Fig. 6(c). It can be seen that the magnetic reversal starts at a corner or edge of the grain due to the inhomogeneous stray field therein [32,90]. The thermal fluctuations make the magnetization contour fluctuate in Fig. 6(c), and add additional fields to induce premature reversal at a corner or edge under even lower external field. It can be seen from Figs. 6(c) that the soft GB layer in models "b" and "c" is magnetically reversed first, followed by the expansion of reversed domains and the

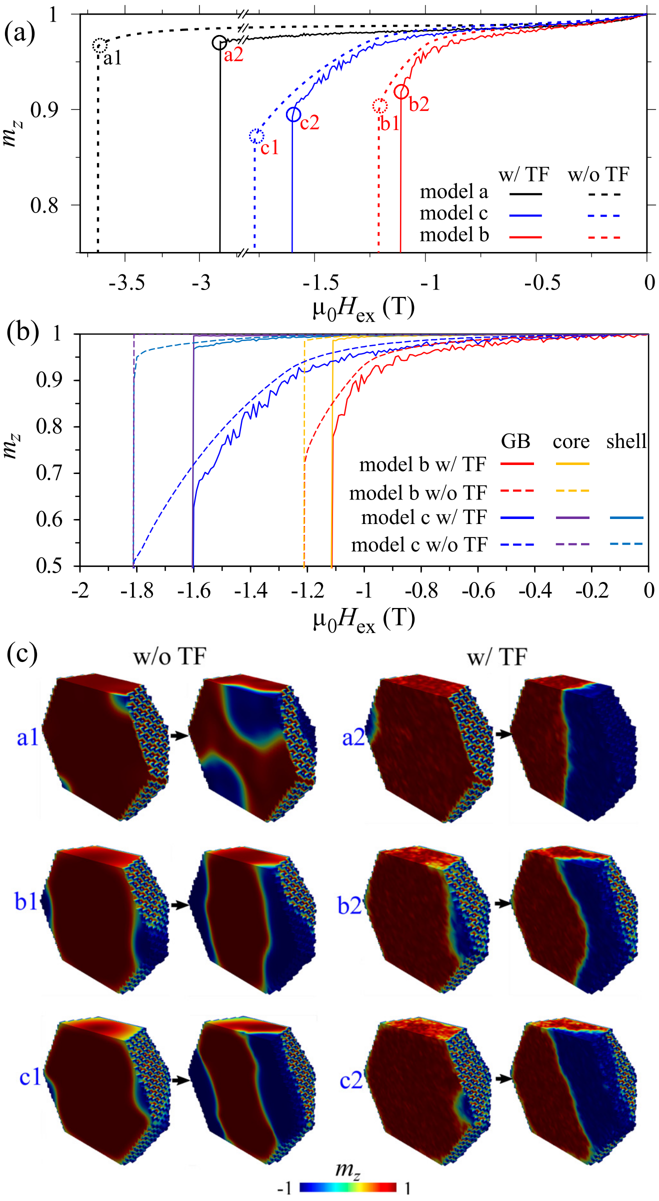

FIG. 6. (a) Total magnetization reversal curves and (b) magnetization curves with separate contributions from the core ($Nd_2Fe_{14}B$), GB, and shell at 400 K with and without thermal fluctuations (TF). The z-component magnetization in (a) and (b) is normalized with respect to its remanent value. (c) Magnetization states at the points marked in (a). 4.5-nm-thick hard shell in model "c." 3-nm-thick defect layer: $\mu_0 M_s^d = 1$ T, $A_e^d = 6.2$ pJ/m, $K_1^d = 0$ MJ/m^3 [40].

propagation of domain walls. This phenomenon is compatible with the exchange-spring behavior [91–93].

Figure 7 presents a quantitative analysis to reveal the influence of thermal fluctuations on both the coercivity and its temperature coefficient β for the three models. As expected, the coercivity rapidly decreases with the increasing temperature, mainly due to the quick decrease of anisotropy field. For the pure $Nd_2Fe_{14}B$ dodecahedral grain (model "a") at different temperatures, it can be found from Fig. 7(a) that the thermal-fluctuations-induced coercivity reduction ($\mu_0 H_{\rm th}$) is around 0.8 T. This 0.8 T reduction of coercivity agrees well with the previous calculation results for a similar grain by Bance *et al.* [41,42], who used the elastic band method or string method to obtain the energy barrier and then determined the thermally activated coercivity. This agreement indicates that our simulation results based on the sLLG equation are credible. In contrast, for models "b" and "c," $\mu_0 H_{\rm th}$ is smaller, around 0.1 and 0.2 T, respectively.

According to the so-called phenomenological global model proposed by Givord *et al.* [94–96],

$$\mu_0 H_{\rm th} = \frac{25 k_{\rm B} T}{v M_{\rm s}}, \tag{7}$$

in which v is the activation volume. Accordingly, $\mu_0 H_{\rm th}$ (proportional to $1/v$) decreases with increasing v. In fact, by using Eq. (7) and $\mu_0 H_{\rm th}$ determined from Fig. 7(a), v can be calculated, as shown in the case of $\mu_0 M_{\rm s}^{\rm d} = 1$ T in Fig. 8. It can be seen that the defect layer leads to a remarkably increased v, which is reduced by adding the hard shell. v is found to decrease in the following order: model "b" > model "c" > model "a," in accordance with the previous study using the energy-barrier method [41]. Therefore, the dependence of v on the model microstructure features could be intrinsically responsible for the different reduction of coercivity by thermal fluctuations ($\mu_0 H_{\rm th} = 0.8$, 0.2, and 0.1 T for models "a," "c," and "b," respectively) in the three models.

We define the coercivity reduction ratio by thermal fluctuations as $\Delta h_{\rm th} = H_{\rm th}/H_{\rm c}^0$, in which $H_{\rm c}^0$ is the coercivity without thermal fluctuations. It can be seen clearly from Fig. 7(b) that $\Delta h_{\rm th}$ increases with the temperature, indicating the stronger intensity of thermal fluctuations at higher temperatures. $H_{\rm c}^0$ is deduced to be proportional to $v^{-2/3}$ [96] and $H_{\rm th}$ to v^{-1}, so $\Delta h_{\rm th}$ is proportional to $v^{-1/3}$. Here, v decreases in the following order: model "b" > model "c" > model "a." Therefore, at the same temperature, $\Delta h_{\rm th}$ is the highest in model "a" and lowest in model "b." For example, $\Delta h_{\rm th}$ increases from 15.3%, 5.1%, and 6.8% at 300 K to 31%, 15.4%, and 16.4% at 500 K for models "a," "b," and "c," respectively.

The temperature coefficient of coercivity, β, is a very important parameter for the performance evaluation of Nd-Fe-B magnets at high temperatures. Here we calculate β by $\beta(T) = \frac{1}{H_{\rm c}} \frac{dH_{\rm c}}{dT}$ [97]. Since the curve $H_{\rm c}$ vs T is found to be almost linear, we estimated $\frac{dH_{\rm c}}{dT}$ by linearly fitting the $H_{\rm c}$ vs T curve. Figure 7(c) presents β as a function of temperature for all three models. β is found to decrease with the increasing temperature. At 300 K, β is around -0.24 to -0.35% K^{-1}. A typical value of β for the hot-deformed Nd-Fe-B magnets and commercial Nd-Fe-B sintered magnets at room temperature is about -0.48 and -0.6% K^{-1}, respectively [7,9]. These β values are smaller than our calculated ones, possibly owing to the ideally simplified microstructure in our simulations. In addition, it is clear in Fig. 7(c) that thermal fluctuations further decrease β and thus make Nd-Fe-B magnets with lower thermal stability. For example, thermal fluctuations reduce β by 0.04 and 0.19% K^{-1} for model "a" at 300 and 450 K, respectively. At 500 K, the reduction of β by thermal fluctuations is 0.3, 0.16, and 0.11% K^{-1} for models "a," "b," and "c," respectively.

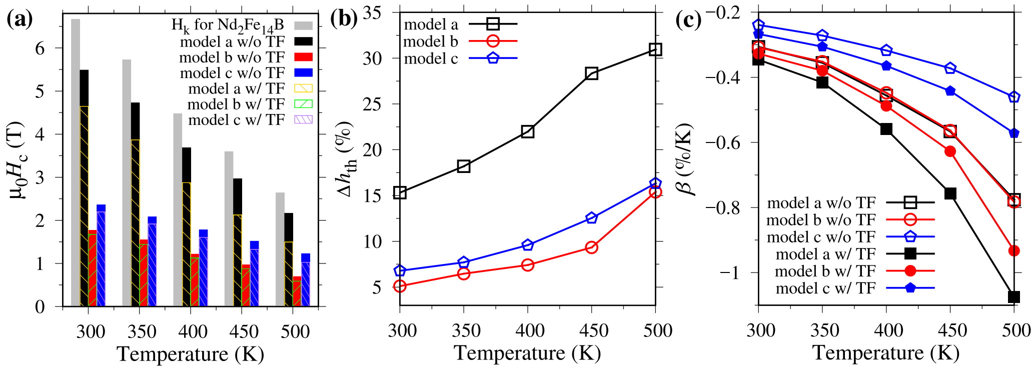

FIG. 7. (a) Coercivity, (b) coercivity reduction ratio ($\Delta h_{\rm th} = H_{\rm th}/H_{\rm c}^0$) by thermal fluctuations (TF), and (c) temperature coefficient of coercivity (β) as a function of temperature for three models. $\beta(T) = \frac{1}{H_{\rm c}(T)}\frac{dH_{\rm c}}{dT}$ in which $\frac{dH_{\rm c}}{dT}$ is the fitted slope of curve $H_{\rm c}$ vs T. The defect layer is 3 nm thick with an Fe+Co content around 60% [40]: $\mu_0 M_{\rm s}^{\rm d} = 1$ T, $A_{\rm e}^{\rm d} = 6.2$ pJ/m, $K_1^{\rm d} = 0$ MJ/m^3. The hard shell is 4.5 nm thick $({\rm Nd}_{0.53}{\rm Dy}_{0.47})_2{\rm Fe}_{14}{\rm B}$ with temperature-dependent magnetic properties from [87].

3. Influence of defect layer

In Nd-Fe-B magnets, the ferromagnetic thin grain boundaries or surface defects are found to be the weak region where the magnetization reversal occurs at a low external magnetic field. This weak region is an important microstructure feature for Nd-Fe-B magnets, and is often modeled as a soft defect layer covering the grain. Its influence on the coercivity at high temperatures will be computationally explored here.

According to the results of model “b” with thermal fluctuations in Fig. 7(a), the introduction of a 3-nm-thick defect layer can significantly reduce the coercivity by 2.9 and 2.4 T at 300 and 350 K, respectively. In contrast, the coercivity reduction is only 1.3 and 0.9 T at 450 and 500 K, respectively. This implies that the defect layer has a much stronger influence on coercivity at lower temperatures. In addition, the defect layer can significantly decrease the influence of thermal fluctuations on coercivity [Fig. 7(b)] and increase the thermal stability [curves with thermal fluctuations in Fig. 7(c)]. The enhanced thermal stability and the reduced influence of thermal fluctuations in model “b” when compared to model “a” are mainly attributed to the large activation volume, which is induced by the defect layer in model “b,” as shown in Fig. 8 and the above discussions based on Eq. (7). The significantly reduced coercivity in model “b” is due to the zero magnetocrystalline anisotropy of the defect layer. Consequently, the defect layer seems like a double-edged sword (increasing the thermal stability while decreasing the coercivity) which could possibly be harnessed for a balance between coercivity and thermal stability.

Figure 9 presents the effect of defect-layer magnetization ($\mu_0 M_{\rm s}^{\rm d}$) on $H_{\rm c}$ and β. According to the experimentally measured magnetization of grain boundary in Nd-Fe-B magnets [40,98], defect layers with strong ($\mu_0 M_{\rm s}^{\rm d} = 1$ T), moderate ($\mu_0 M_{\rm s}^{\rm d} = 0.65$ T), and weak ($\mu_0 M_{\rm s}^{\rm d} = 0.15$ T) magnetization are considered. The corresponding exchange stiffness is estimated by $A_{\rm e}^{\rm d} \sim \epsilon(\mu_0 M_{\rm s}^{\rm d})^2$ with the material constant $\epsilon = 5.41$ pJ/m/T^2 which is calculated from the experimental results of α-Fe [40]. It is evident in Fig. 9(a) that weaker magnetization in the defect layer leads to higher coercivity, while a faster decrease of coercivity with respect to temperature. This finding is in accordance with the micromagnetic theoretical analysis, i.e., in the case of defect-layer thickness

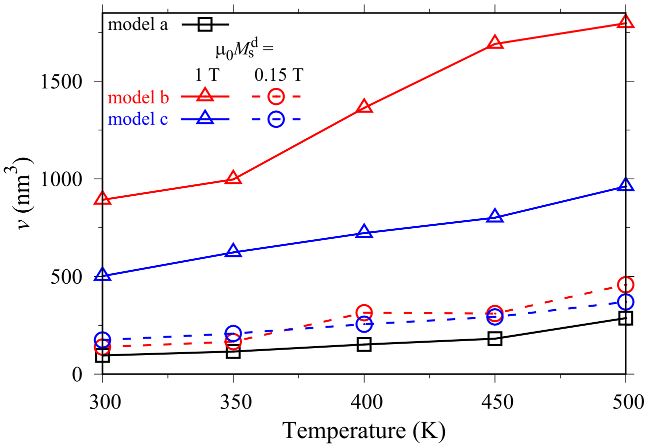

FIG. 8. Temperature-dependent activation volume (v) for different models with very strong magnetization ($\mu_0 M_{\rm s}^{\rm d} = 1$ T) and very weak magnetization ($\mu_0 M_{\rm s}^{\rm d} = 0.15$ T) in the defect layer. The hard-shell thickness in model “c” is 4.5 nm.

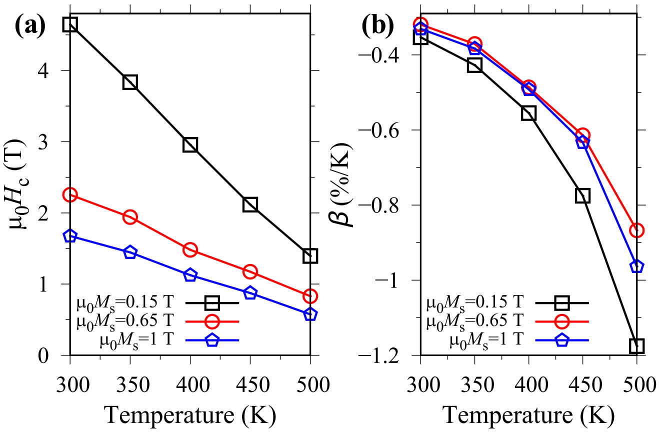

FIG. 9. (a) Coercivity ($\mu_0 H_{\rm c}$) and (b) temperature coefficient of coercivity (β) in model “b” (Fig. 2) with different defect-layer property.

(3 nm here) less than the domain-wall width [Fig. 4(c)], both the nucleation and depinning field are inverse proportional to $\mu_0 M_s^d$ [91,99]. From the temperature coefficient results in Fig. 9(b), it is found that weak magnetization ($\mu_0 M_s^d = 0.15$ T) in the defect layer leads to lower thermal stability than strong ($\mu_0 M_s^d = 1$ T) and moderate ($\mu_0 M_s^d = 0.65$ T) magnetization. The difference in β values for the case of $\mu_0 M_s^d = 1$ and 0.65 T is not significant. These results indicate that an increase of defect-layer magnetization above a certain value (e.g., 0.65 T here) will reduce H_c as usual, but will not considerably influence β.

The defect-layer magnetization is also shown to influence the activation volume in Fig. 8. In both models "b" and "c," the introduction of strong magnetization ($\mu_0 M_s^d = 1$ T) in the defect layer increases the activation volume by several times. In contrast, a weak magnetization of $\mu_0 M_s^d = 0.15$ T only slightly enhances the activation volume.

4. *Influence of hard shell*

It is expected that Dy substitution near grain surfaces effectively enhances coercivity. This idea has been realized by the grain-boundary diffusion of Dy to form a hard shell around the grain surface [10–13]. So the Dy-rich hard shell is another important microstructure feature for high-performance Nd-Fe-B magnets, as illustrated in Fig. 2(c). Currently, it is still essential for Nd-Fe-B magnets used at high temperatures.

As shown for the results of model "c" in Fig. 7(a), adding a 4.5-nm-thick $(Nd_{0.53}Dy_{0.47})_2Fe_{14}B$ hard shell enhances the coercivity by ~0.5 T when compared to model "b" only with a 3-nm-thick defect layer. But the 4.5-nm-thick shell cannot fully cancel out the reduction of coercivity from the 3.5-nm-thick defect layer. In addition, the hard shell remarkably enhances β and thus the thermal stability [Fig. 7(c)], in accordance with the strategy of designing the high-temperature Nd-Fe-B magnets by adding Dy.

As for the activation volume v in Fig. 8, in the case of strong defect-layer magnetization ($\mu_0 M_s^d = 1$ T), adding a 4.5-nm-thick hard shell approximately reduces v by half. However, if the defect-layer magnetization is very weak (e.g., $\mu_0 M_s^d = 0.15$ T), the hard shell shows no significant influence on v (circle markers in Fig. 8). This suggests that decreasing the defect-layer magnetization and meanwhile adding the hard shell not only appreciably increases the coercivity, but also suppresses the thermal-fluctuations-induced coercivity reduction.

Figure 10 shows the dependence of coercivity, thermal stability, and activation volume on the shell thickness (t^{sh}). The dashed line in Fig. 10(a) shows the coercivity when the core is assumed to have the same properties as the shell, corresponding to the limit of a very thick shell. In Fig. 10(a), the coercivity is first improved by increasing t^{sh} and then saturates toward the dashed line at around $t^{sh} = 6$–8 nm. Similarly, the temperature coefficient of coercivity increases with t^{sh} and does not change significantly after t^{sh} exceeds 6–8 nm, as shown in Fig. 10(b). The activation volume in Fig. 10(c) is found to not remarkably change with t^{sh}, indicating a weak dependence of the thermal-fluctuations-induced coercivity reduction on the hard-shell thickness. These results imply that a shell thickness of $t^{sh} = 6$–8 nm is enough to achieve the maximum coercivity enhancement and thermal stability, and adding Dy into the core (e.g., Dy alloying in the initial sintered magnets before grain boundary diffusion) is not indispensable.

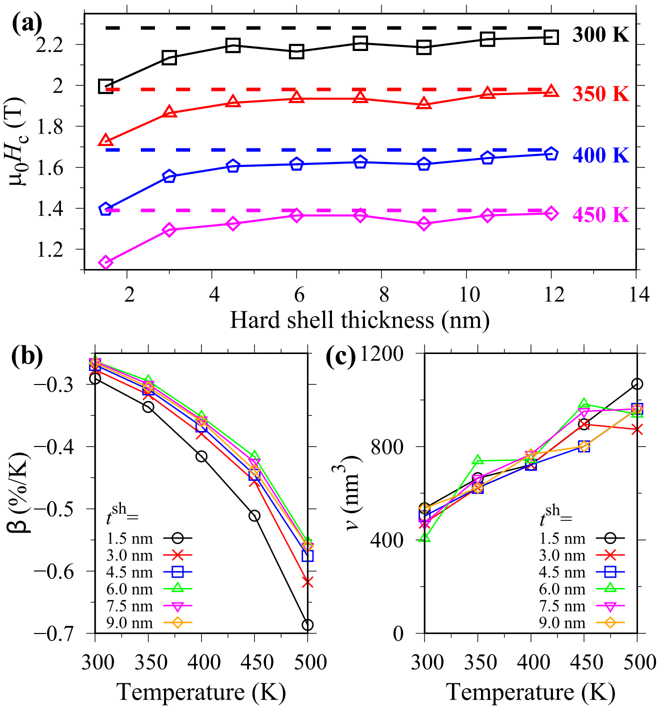

FIG. 10. (a) Coercivity, (b) temperature coefficient of coercivity (β), and (c) activation volume (v) as a function of the hard-shell thickness (t^{sh}) in model "c" (Fig. 2) at different temperatures. Dashed lines in (a) correspond to the results when the core takes the same properties as the shell and $t^{sh} = 4.5$ nm. 3-nm-thick defect layer: $\mu_0 M_s^d = 1$ T, $A_e^d = 6.2$ pJ/m, $K_1^d = 0$ MJ/m^3 [40].

IV. CONCLUSIONS

In summary, we have performed a multiscale study on the calculation of coercivity in Nd-Fe-B permanent magnets at high temperatures by combining the atomistic spin model (ASM) and micromagnetic simulations. Using the ASM Hamiltonian constructed for $Nd_2Fe_{14}B$, we carry out ASM simulations to obtain the temperature-dependent saturated magnetization $M_s(T)$, magnetocrystalline anisotropy $K_1(T)$, and exchange stiffness constant $A_e(T)$ at high temperatures. The calculated $M_s(T)$, $K_1(T)$, and $A_e(T)$ are demonstrated to coincide with the experimental measurement.

Taking the ASM results as input, finite-temperature micromagnetic simulations using the stochastic Landau-Lifshitz-Gilbert equation are performed to calculate the magnetic reversal, thermal-activation volume v, thermal-fluctuations-induced coercivity reduction H_{th} and its ratio Δh_{th}, and coercivity H_c and its temperature coefficient β in a pure $Nd_2Fe_{14}B$ and $Nd_2Fe_{14}B$ grain with surface defect layer or Dy-rich hard shell. Specifically, the stepwise external field and the step time for calculating the magnetic reversal curves are optimized. It is found that apart from the anisotropy field decreasing with temperature, the thermal fluctuations further reduce H_c by 5–10% and β by 0.02–0.1% K^{-1}. The defect layer with strong magnetization (e.g., 1 T) is demonstrated to result in a remarkably increased v (which can be reduced by adding the Dy-rich hard shell) and significantly decreased H_c, while suppressing the influence of thermal fluctuations and thus reducing H_{th} and Δh_{th}. It is also revealed that even though the presence of a Dy-rich hard shell cannot fully cancel out the reduction of coercivity from the defect layer, a 4.5-nm-thick $(Nd_{0.53}Dy_{0.47})_2Fe_{14}B$ shell enhances H_c by 0.5 T and considerably improves the thermal stability. Both H_c and β are found to saturate at a Dy-rich shell thickness of 6–8 nm. A even thicker shell or Dy alloying into the core prior to grain-boundary diffusion is not necessary.

The multiscale scheme and the calculation results are useful for the design of high-performance Nd-Fe-B permanent magnets used at high temperatures in terms of microstructure engineering.

ACKNOWLEDGMENTS

The support from the German Science Foundation (Grants No. DFG YI 165/1-1 and No. DFG XU 121/7-1) and the German federal state of Hessen through its excellence programme LOEWE RESPONSE is appreciated. M.Y. acknowledges the support from the open project of the State Key Laboratory for Strength and Vibration of Mechanical Structures (Grant No. SV2017-KF-28), the 15th Thousand Youth Talents Program of China, the Research Fund of the State Key Laboratory of Mechanics and Control of Mechanical Structures (Grant No. MCMS-I-0419G01), and a project funded by the Priority Academic Program Development of Jiangsu Higher Education Institutions. The authors also acknowledge the access to the Lichtenberg High Performance Computer of TU Darmstadt.

[1] M. Sagawa, S. Fujimura, N. Togawa, H. Yamamoto, and Y. Matsuura, New material for permanent magnets on a base of Nd and Fe, J. Appl. Phys. **55**, 2083 (1984).

[2] J. J. Croat, J. F. Herbst, R. W. Lee, and F. E. Pinkerton, High-energy product Nd-Fe-B permanent magnets, Appl. Phys. Lett. **44**, 148 (1984).

[3] Y. Xiao, S. Liu, H. F. Mildrum, K. J. Strnat, and A. E. Ray, The effects of various alloying elements on modifying the elevated temperature magnetic properties of sintered Nd-Fe-B magnets, J. Appl. Phys. **63**, 3516 (1988).

[4] L. Q. Yu, J. Zhang, S. Q. Hu, Z. D. Han, and M. Yan, Production for high thermal stability NdFeB magnets, J. Magn. Magn. Mater. **320**, 1427 (2008).

[5] M. H. Ghandehari, Reactivity of Dy_2O_3 and Tb_4O_7 with $Nd_{15}Fe_{77}B_8$ powder and the coercivity of the sintered magnets, Appl. Phys. Lett. **48**, 548 (1986).

[6] X. G. Cui, C. Y. Cui, X. N. Cheng, and X. J. Xu, Effect of Dy_2O_3 intergranular addition on thermal stability and corrosion resistance of Nd-Fe-B magnets, Intermetallics **55**, 118 (2014).

[7] J. Liu, H. Sepehri-Amin, T. Ohkubo, K. Hioki, A. Hattori, T. Schrefl, and K. Hono, Grain size dependence of coercivity of hot-deformed Nd-Fe-B anisotropic magnets, Acta Mater. **82**, 336 (2015).

[8] H. Sepehri-Amin, T. Ohkubo, S. Nagashima, M. Yano, T. Shoji, A. Kato, T. Schrefl, and K. Hono, High-coercivity ultrafine-grained anisotropic Nd-Fe-B magnets processed by hot deformation and the Nd-Cu grain boundary diffusion process, Acta Mater. **61**, 6622 (2013).

[9] H. Sepehri-Amin, L. Liu, T. Ohkubo, M. Yano, T. Shoji, A. Kato, T. Schrefl, and K. Hono, Microstructure and temperature dependent of coercivity of hot-deformed Nd-Fe-B magnets diffusion processed with Pr-Cu alloy, Acta Mater. **99**, 297 (2015).

[10] K. Hirota, H. Nakamura, T. Minowa, and M. Honshima, Coercivity enhancement by the grain boundary diffusion process to Nd-Fe-B sintered magnets, IEEE Trans. Magn. **42**, 2909 (2006).

[11] H. Sepehri-Amin, T. Ohkubo, and K. Hono, The mechanism of coercivity enhancement by the grain boundary diffusion process of Nd-Fe-B sintered magnets, Acta Mater. **61**, 1982 (2013).

[12] S. Sawatzki, C. Kübel, S. Ener, and O. Gutfleisch, Grain boundary diffusion in nanocrystalline Nd-Fe-B permanent magnets with low-melting eutectics, Acta Mater. **115**, 354 (2016).

[13] K. Löewe, C. Brombacher, M. Katter, and O. Gutfleisch, Temperature-dependent Dy diffusion processes in Nd-Fe-B permanent magnets, Acta Mater. **83**, 248 (2015).

[14] X. B. Liu and Z. Altounian, The partitioning of Dy and Tb in NdFeB magnets: A first-principles study, J. Appl. Phys. **111**, 07A701 (2012).

[15] Y. Toga, T. Suzuki, and A. Sakuma, Effects of trace elements on the crystal field parameters of Nd ions at the surface of $Nd_2Fe_{14}B$ grains, J. Appl. Phys. **117**, 223905 (2015).

[16] T. Suzuki, Y. Toga, and A. Sakuma, Effects of deformation on the crystal field parameter of the Nd ions in $Nd_2Fe_{14}B$, J. Appl. Phys. **115**, 17A703 (2014).

[17] Y. Tatetsu, S. Tsuneyuki, and Y. Gohda, First-Principles Study of the Role of Cu in Improving the Coercivity of Nd-Fe-B Permanent Magnets, Phys. Rev. Appl. **6**, 064029 (2016).

[18] M. Yi, H. Zhang, O. Gutfleisch, and B.-X. Xu, Multiscale Examination of Strain Effects in Nd-Fe-B Permanent Magnets, Phys. Rev. Appl. **8**, 014011 (2017).

[19] H. Tsuchiura, T. Yoshioka, and P. Novak, First-principles calculations of crystal field parameters of Nd ions near surfaces and interfaces in Nd-Fe-B magnets, IEEE Trans. Magn. **50**, 1 (2014).

[20] R. F. L. Evans, D. Givord, R. Cuadrado, T. Shoji, M. Yano, M. Ito, A. Manabe, G. Hrkac, T. Schrefl, and R. W. Chantrell, Atomistic spin dynamics and temperature dependent properties of $Nd_2Fe_{14}B$, in *8th Joint European Magnetic Symposia, 21-26 August, 2016* (unpublished).

[21] Y. Toga, M. Matsumoto, S. Miyashita, H. Akai, S. Doi, T. Miyake, and A. Sakuma, Monte Carlo analysis for finite-temperature magnetism of $Nd_2Fe_{14}B$ permanent magnet, Phys. Rev. B **94**, 174433 (2016).

[22] M. Nishino, Y. Toga, S. Miyashita, H. Akai, A. Sakuma, and S. Hirosawa, Atomistic-model study of temperature-dependent domain walls in the neodymium permanent magnet $Nd_2Fe_{14}B$, Phys. Rev. B **95**, 094429 (2017).

[23] S. C. Westmoreland, R. F. L. Evans, G. Hrkac, T. Schrefl, G. T. Zimanyi, M. Winklhofer, N. Sakuma, M. Yano, A. Kato,

T. Shoji, A. Manabe, M. Ito, and R. W. Chantrell, Multiscale model approaches to the design of advanced permanent magnets, Scr. Mater. **148**, 56 (2018).

[24] H. Tsuchiura, T. Yoshioka, and P. Novák, Bridging atomistic magnetism and coercivity in Nd-Fe-B magnets, Scr. Mater. **154**, 248 (2018).

[25] S. Miyashita, M. Nishino, Y. Toga, T. Hinokihara, T. Miyake, S. Hirosawa, and A. Sakuma, Perspectives of stochastic micromagnetism of $Nd_2Fe_{14}B$ and computation of thermally activated reversal process, Scr. Mater. **154**, 259 (2018).

[26] Y. Toga, M. Nishino, S. Miyashita, T. Miyake, and A. Sakuma, Anisotropy of exchange stiffness based on atomic-scale magnetic properties in the rare-earth permanent magnet $Nd_2Fe_{14}B$, Phys. Rev. B **98**, 054418 (2018).

[27] Q. Gong, M. Yi, R. F. L. Evans, B.-X. Xu, and O. Gutfleisch, Calculating temperature-dependent properties of $Nd_2Fe_{14}B$ permanent magnets by atomistic spin model simulations, Phys. Rev. B **99**, 214409 (2019).

[28] B. Skubic, J. Hellsvik, L. Nordström, and O. Eriksson, A method for atomistic spin dynamics simulations: Implementation and examples, J. Phys.: Condens. Matter **20**, 315203 (2008).

[29] R. F. L. Evans, W. J. Fan, P. Chureemart, T. A. Ostler, M. O. A. Ellis, and R. W. Chantrell, Atomistic spin model simulations of magnetic nanomaterials, J. Phys.: Condens. Matter **26**, 103202 (2014).

[30] O. Eriksson, A. Bergman, L. Bergqvist, and J. Hellsvik, *Atomistic Spin Dynamics: Foundations and Applications* (Oxford University Press, Oxford, 2017).

[31] H. Sepehri-Amin, T. Ohkubo, M. Gruber, T. Schrefl, and K. Hono, Micromagnetic simulations on the grain size dependence of coercivity in anisotropic Nd-Fe-B sintered magnets, Scr. Mater. **89**, 29 (2014).

[32] M. Yi, O. Gutfleisch, and B.-X. Xu, Micromagnetic simulations on the grain shape effect in Nd-Fe-B magnets, J. Appl. Phys. **120**, 033903 (2016).

[33] S. Erokhin and D. Berkov, Optimization of Nanocomposite Materials for Permanent Magnets: Micromagnetic Simulations of the Effects of Intergrain Exchange and the Shapes of Hard Grains, Phys. Rev. Appl. **7**, 014011 (2017).

[34] J. Fidler and T. Schrefl, Micromagnetic modeling-the current state of the art, J. Phys. D **33**, R135 (2000).

[35] G. Hrkac, T. G. Woodcock, C. Freeman, A. Goncharov, J. Dean, T. Schrefl, and O. Gutfleisch, The role of local anisotropy profiles at grain boundaries on the coercivity of $Nd_2Fe_{14}B$ magnets, Appl. Phys. Lett. **97**, 232511 (2010).

[36] T. G. Woodcock, Y. Zhang, G. Hrkac, G. Ciuta, N. M. Dempsey, T. Schrefl, O. Gutfleisch, and D. Givord, Understanding the microstructure and coercivity of high performance NdFeB-based magnets, Scr. Mater. **67**, 536 (2012).

[37] J. Fischbacher, A. Kovacs, M. Gusenbauer, H. Oezelt, L. Exl, S. Bance, and T. Schrefl, Micromagnetics of rare-earth efficient permanent magnets, J. Phys. D **51**, 193002 (2018).

[38] P. Toson, G. A. Zickler, and J. Fidler, Do micromagnetic simulations correctly predict hard magnetic hysteresis properties? Physica B (Amsterdam) **486**, 142 (2016).

[39] T. Helbig, K. Loewe, S. Sawatzki, M. Yi, B.-X. Xu, and O. Gutfleisch, Experimental and computational analysis of magnetization reversal in (Nd, Dy)-Fe-B core shell sintered magnets, Acta Mater. **127**, 498 (2017).

[40] G. A. Zickler, J. Fidler, J. Bernardi, T. Schrefl, and A. Asali, A combined TEM/STEM and micromagnetic study of the anisotropic nature of grain boundaries and coercivity in Nd-Fe-B magnets, Adv. Mater. Sci. Eng. **2017**, 6412042 (2017).

[41] S. Bance, J. Fischbacher, and T. Schrefl, Thermally activated coercivity in core-shell permanent magnets, J. Appl. Phys. **117**, 17A733 (2015).

[42] S. Bance, J. Fischbacher, A. Kovacs, H. Oezelt, F. Reichel, and T. Schrefl, Thermal activation in permanent magnets, JOM **67**, 1350 (2015).

[43] H. Kronmüller, K.-D. Durst, and M. Sagawa, Analysis of the magnetic hardening mechanism in RE-FeB permanent magnets, J. Magn. Magn. Mater. **74**, 291 (1988).

[44] T. Oikawa, H. Yokota, T. Ohkubo, and K. Hono, Large-scale micromagnetic simulation of Nd-Fe-B sintered magnets with Dy-rich shell structures, AIP Adv. **6**, 056006 (2016).

[45] J. Thielsch, D. Suess, L. Schultz, and O. Gutfleisch, Dependence of coercivity on length ratios in sub-micron $Nd_2Fe_{14}B$ particles with rectangular prism shape, J. Appl. Phys. **114**, 223909 (2013).

[46] S. Bance, B. Seebacher, T. Schrefl, L. Exl, M. Winklhofer, G. Hrkac, G. Zimanyi, T. Shoji, M. Yano, N. Sakuma *et al.*, Grain-size dependent demagnetizing factors in permanent magnets, J. Appl. Phys. **116**, 233903 (2014).

[47] R. Fischer, T. Schrefl, H. Kronmüller, and J. Fidler, Grain-size dependence of remanence and coercive field of isotropic nanocrystalline composite permanent magnets, J. Magn. Magn. Mater. **153**, 35 (1996).

[48] R. Ramesh, G. Thomas, and B. M. Ma, Magnetization reversal in nucleation controlled magnets. II. Effect of grain size and size distribution on intrinsic coercivity of Fe-Nd-B magnets, J. Appl. Phys. **64**, 6416 (1988).

[49] K. Uestuener, M. Katter, and W. Rodewald, Dependence of the mean grain size and coercivity of sintered Nd–Fe–B magnets on the initial powder particle size, IEEE Trans. Magn. **42**, 2897 (2006).

[50] G. Henkelman, B. P. Uberuaga, and H. Jónsson, A climbing image nudged elastic band method for finding saddle points and minimum energy paths, J. Chem. Phys. **113**, 9901 (2000).

[51] R. Dittrich, T. Schrefl, D. Suess, W. Scholz, H. Forster, and J. Fidler, A path method for finding energy barriers and minimum energy paths in complex micromagnetic systems, J. Magn. Magn. Mater. **250**, 12 (2002).

[52] M. F. Carilli, K. T. Delaney, and G. H. Fredrickson, Truncation-based energy weighting string method for efficiently resolving small energy barriers, J. Chem. Phys. **143**, 054105 (2015).

[53] E. Weinan, W. Ren, and E. Vanden-Eijnden, String method for the study of rare events, Phys. Rev. B **66**, 052301 (2002).

[54] Q. Du and L. Zhang, A constrained string method and its numerical analysis, Commun. Math. Sci. **7**, 1039 (2009).

[55] A. Samanta and E. Weinan, Optimization-based string method for finding minimum energy path, Commun. Comput. Phys. **14**, 265 (2013).

[56] W. Ren and E. Vanden-Eijnden, A climbing string method for saddle point search, J. Chem. Phys. **138**, 134105 (2013).

[57] J. Fischbacher, A. Kovacs, H. Oezelt, M. Gusenbauer, T. Schrefl, L. Exl, D. Givord, N. M. Dempsey, G. Zimanyi, M. Winklhofer *et al.*, On the limits of coercivity in permanent magnets, Appl. Phys. Lett. **111**, 072404 (2017).

[58] W. F. Brown Jr, Thermal fluctuations of a single-domain particle, Phys. Rev. **130**, 1677 (1963).

[59] W. Scholz, T. Schrefl, and J. Fidler, Micromagnetic simulation of thermally activated switching in fine particles, J. Magn. Magn. Mater. **233**, 296 (2001).

[60] T. Schrefl, W. Scholz, D. Süss, and J. Fidler, Computational micromagnetics: Prediction of time dependent and thermal properties, J. Magn. Magn. Mater. **226–230**, 1213 (2001).

[61] D. V. Berkov, Fast switching of magnetic nanoparticles: Simulation of thermal noise effects using the langevin dynamics, IEEE Trans. Magn. **38**, 2489 (2002).

[62] V. Tsiantos, W. Scholz, D. Suess, T. Schrefl, and J. Fidler, The effect of the cell size in Langevin micromagnetic simulations, J. Magn. Magn. Mater. **242–245**, 999 (2002).

[63] E. Martinez, L. Lopez-Diaz, L. Torres, and C. J. Garcia-Cervera, Micromagnetic simulations with thermal noise: Physical and numerical aspects, J. Magn. Magn. Mater. **316**, 269 (2007).

[64] E. Martínez, L. Lopez-Diaz, L. Torres, and C. J. Garcia-Cervera, Minimizing cell size dependence in micromagnetics simulations with thermal noise, J. Phys. D **40**, 942 (2007).

[65] M. Yamada, H. Kato, H. Yamamoto, and Y. Nakagawa, Crystal-field analysis of the magnetization process in a series of $Nd_2Fe_{14}B$-type compounds, Phys. Rev. B **38**, 620 (1988).

[66] R. J. Elliott and K. W. H. Stevens, The theory of magnetic resonance experiments on salts of the rare earths, Proc. R. Soc. London A **218**, 553 (1953).

[67] A. J. Freeman and R. E. Watson, Theoretical investigation of some magnetic and spectroscopic properties of rare-earth ions, Phys. Rev. **127**, 2058 (1962).

[68] Y. Miura, H. Tsuchiura, and T. Yoshioka, Magnetocrystalline anisotropy of the Fe-sublattice in $Y_2Fe_{14}B$ systems, J. Appl. Phys. **115**, 17A765 (2014).

[69] A. I. Liechtenstein, M. I. Katsnelson, V. P. Antropov, and V. A. Gubanov, Local spin density functional approach to the theory of exchange interactions in ferromagnetic metals and alloys, J. Magn. Magn. Mater. **67**, 65 (1987).

[70] M. J. Han, T. Ozaki, and J. Yu, Electronic structure, magnetic interactions, and the role of ligands in Mn_n (n=4,12) single-molecule magnets, Phys. Rev. B **70**, 184421 (2004).

[71] H. Yoon, T. J. Kim, J.-H. Sim, S. W. Jang, T. Ozaki, and M. J. Han, Reliability and applicability of magnetic-force linear response theory: Numerical parameters, predictability, and orbital resolution, Phys. Rev. B **97**, 125132 (2018).

[72] R. Cardias, A. Szilva, A. Bergman, I. Di Marco, M. I. Katsnelson, A. I. Lichtenstein, L. Nordström, A. B. Klautau, O. Eriksson, and Y. O. Kvashnin, The Bethe-Slater curve revisited; new insights from electronic structure theory, Sci. Rep. **7**, 4058 (2017).

[73] K.-D. Durst and H. Kronmüller, Determination of intrinsic magnetic material parameters of $Nd_2Fe_{14}B$ from magnetic measurements of sintered $Nd_{15}Fe_{77}B_8$ magnets, J. Magn. Magn. Mater. **59**, 86 (1986).

[74] S. Hirosawa, Y. Matsuura, H. Yamamoto, S. Fujimura, M. Sagawa, and H. Yamauchi, Magnetization and magnetic anisotropy of $R_2Fe_{14}B$ measured on single crystals, J. Appl. Phys. **59**, 873 (1986).

[75] D. Givord, H. S. Li, and R. de la Bąthie, Magnetic properties of $Y_2Fe_{14}B$ and $Nd_2Fe_{14}B$ single crystals, Solid State Commun. **88**, 907 (1993).

[76] A. Szilva, M. Costa, A. Bergman, L. Szunyogh, L. Nordström, and O. Eriksson, Interatomic Exchange Interactions for Finite-Temperature Magnetism and Nonequilibrium Spin Dynamics, Phys. Rev. Lett. **111**, 127204 (2013).

[77] Y. O. Kvashnin, R. Cardias, A. Szilva, I. Di Marco, M. I. Katsnelson, A. I. Lichtenstein, L. Nordström, A. B. Klautau, and O. Eriksson, Microscopic Origin of Heisenberg and Non-Heisenberg Exchange Interactions in Ferromagnetic Bcc Fe, Phys. Rev. Lett. **116**, 217202 (2016).

[78] D. Miura and A. Sakuma, Non-collinearity effects on magnetocrystalline anisotropy for $R_2Fe_{14}B$ magnets, J. Phys. Soc. Jpn. **88**, 044804 (2017).

[79] P. Asselin, R. F. L. Evans, J. Barker, R. W. Chantrell, R. Yanes, O. Chubykalo-Fesenko, D. Hinzke, and U. Nowak, Constrained Monte Carlo method and calculation of the temperature dependence of magnetic anisotropy, Phys. Rev. B **82**, 054415 (2010).

[80] H. Kronmüller and M. Fähnle, *Micromagnetism and the Microstructure of Ferromagnetic Solids* (Cambridge University Press, Cambridge, 2003).

[81] W. F. Brown Jr, Micromagnetics: Successor to domain theory? J. Phys. Radium **20**, 101 (1959).

[82] T. L. Gilbert, A phenomenological theory of damping in ferromagnetic materials, IEEE Trans. Magn. **40**, 3443 (2004).

[83] M. Yi and B.-X. Xu, A constraint-free phase field model for ferromagnetic domain evolution, Proc. R. Soc. London A **470**, 20140517 (2014).

[84] A. Vansteenkiste, J. Leliaert, M. Dvornik, M. Helsen, F. Garcia-Sanchez, and B. Van Waeyenberge, The design and verification of MuMax3, AIP Adv. **4**, 107133 (2014).

[85] J. Leliaert, J. Mulkers, J. De Clercq, A. Coene, M. Dvornik, and B. Van Waeyenberge, Adaptively time stepping the stochastic Landau-Lifshitz-Gilbert equation at nonzero temperature: Implementation and validation in MuMax3, AIP Adv. **7**, 125010 (2017).

[86] W. Rave, K. Ramstöck, and A. Hubert, Corners and nucleation in micromagnetics1, J. Magn. Magn. Mater. **183**, 329 (1998).

[87] M. Sagawa, S. Hirosawa, K. Tokuhara, H. Yamamoto, S. Fujimura, Y. Tsubokawa, and R. Shimizu, Dependence of coercivity on the anisotropy field in the $Nd_2Fe_{14}B$-type sintered magnets, J. Appl. Phys. **61**, 3559 (1987).

[88] J. Crangle and G. M. Goodman, The magnetization of pure iron and nickel, Proc. R. Soc. London A **321**, 477 (1971).

[89] T. Nakamura, A. Yasui, Y. Kotani, T. Fukagawa, T. Nishiuchi, H. Iwai, T. Akiya, T. Ohkubo, Y. Gohda, K. Hono *et al.*, Direct observation of ferromagnetism in grain boundary phase of Nd-Fe-B sintered magnet using soft x-ray magnetic circular dichroism, Appl. Phys. Lett. **105**, 202404 (2014).

[90] T. Schrefl, J. Fidler, and H. Kronmüller, Nucleation fields of hard magnetic particles in 2D and 3D micromagnetic calculations, J. Magn. Magn. Mater. **138**, 15 (1994).

[91] R. Skomski and J. M. D. Coey, Giant energy product in nanostructured two-phase magnets, Phys. Rev. B **48**, 15812 (1993).

[92] R. Skomski, Nanomagnetics, J. Phys.: Condens. Matter **15**, R841 (2003).

[93] E. F. Kneller and R. Hawig, The exchange-spring magnet: A new material principle for permanent magnets, IEEE Trans. Magn. **27**, 3588 (1991).

[94] D. Givord, A. Lienard, P. Tenaud, and T. Viadieu, Magnetic viscosity in Nd-Fe-B sintered magnets, J. Magn. Magn. Mater. **67**, L281 (1987).

[95] D. Givord, P. Tenaud, and T. Viadieu, Coercivity mechanisms in ferrites and rare earth transition metal sintered magnets ($SmCo_5$, Nd-Fe-B), IEEE Trans. Magn. **24**, 1921 (1988).

[96] D. Givord, Q. Lu, M. F. Rossignol, P. Tenaud, and T. Viadieu, Experimental approach to coercivity analysis in hard magnetic materials, J. Magn. Magn. Mater. **83**, 183 (1990).

[97] S. Liu and G. E. Kuhl, Temperature coefficients of rare earth permanent magnets, IEEE Trans. Magn. **35**, 3271 (1999).

[98] G. A. Zickler and J. Fidler, Nanocompositional electron microscopic analysis and role of grain boundary phase of isotropically oriented Nd-Fe-B magnets, Adv. Mater. Sci. Eng. **2017**, 1461835 (2017).

[99] H. Kronmüller and D. Goll, Micromagnetic theory of the pinning of domain walls at phase boundaries, Physica B (Amsterdam) **319**, 122 (2002).